

Optical Engineering

SPIEDigitalLibrary.org/oe

Illumination-invariant phase-shifting algorithm for three-dimensional profilometry of a moving object

Fuqin Deng
Chang Liu
Wuifung Sze
Jiangwen Deng
Kenneth S. M. Fung
Winghong Leung
Edmund Y. Lam



Illumination-invariant phase-shifting algorithm for three-dimensional profilometry of a moving object

Fuqin Deng

University of Hong Kong
Imaging Systems Laboratory
Department of Electrical and Electronic
Engineering
Pokfulam Road, Hong Kong
and
ASM Pacific Technology Limited
Kwai Chung, Hong Kong

Chang Liu

Wuifung Sze

Jiangwen Deng

Kenneth S. M. Fung

Winghong Leung

ASM Pacific Technology Limited
Kwai Chung, Hong Kong

Edmund Y. Lam

University of Hong Kong
Imaging Systems Laboratory
Department of Electrical and Electronic
Engineering
Pokfulam Road, Hong Kong
E-mail: elam@eee.hku.hk

Abstract. Uneven illumination is a common problem in practical optical systems designed for machine vision applications, and it leads to significant errors when phase-shifting algorithms (PSA) are used to reconstruct the surface of a moving object. We propose an illumination-reflectivity-focus model to characterize this uneven illumination effect on phase-measuring profilometry. With this model, we separate the illumination factor effectively and consider the phase reconstruction from an optimization perspective. Furthermore, we formulate an illumination-invariant phase-shifting algorithm (II-PSA) to reconstruct the surface of a moving object under an uneven illumination environment. Experimental results show that it can improve the reconstruction quality both visually and numerically. © 2012 Society of Photo-Optical Instrumentation Engineers (SPIE). [DOI: [10.1117/1.OE.51.9.097001](https://doi.org/10.1117/1.OE.51.9.097001)]

Subject terms: three-dimensional image acquisition; industrial inspection; surface measurements; profilometry.

Paper 120214P received Feb. 19, 2012; revised manuscript received Aug. 20, 2012; accepted for publication Aug. 20, 2012; published online Sep. 13, 2012; corrected Sep. 18, 2012.

1 Introduction

Over the past few years, advances in surface reconstruction have inspired many applications.¹ However, surface profiling is particularly challenging when it is applied to the semiconductor industry, due to two conflicting requirements: a small feature size requiring a high precision, and the need for a high throughput.² Application-specific solutions are often needed. For example, to tackle certain applications with strict constraints on the dimension of the system, Wakayama and Yoshizawa developed a compact camera for three-dimensional profilometry.³ On the other hand, for some inspection applications, explicit three-dimensional reconstruction is not needed, but efficiency is often of prime concern. As another example, Dong et al. proposed a biplanar disparity matrix for measuring the heights of wafer bumps based on a specially designed illumination and imaging setup.⁴ Nevertheless, in many other applications such as surface inspection and volume measurement, a dense profile is necessary, so good ways to reconstruct the full surface profile are needed.⁵

Phase-measuring profilometry, especially the phase-shifting algorithm (PSA), is one of the most popular methods for dense surface reconstruction. By projecting a sinusoidal pattern with different phase shifts on to a stationary surface and analyzing the corresponding fringe pattern images, one can recover the phase offset due to the height variation of the surface. When it is combined with an encoded marker as the reference, one can obtain high-resolution, three-dimensional

absolute coordinates of the surface.⁶ Besides using PSA with a sinusoidal pattern for three-dimensional profilometry, Cheng et al. developed a method that projects binary patterns on the surfaces of integrated circuit (IC) samples⁷ and optimizes the bit-pairing codification to obtain robust profile data.⁸ However, one requirement of this technique is an additional interpolation step to obtain a dense surface of the object due to the discrete nature of the patterns. PSA also requires a lot of computation, but it can be efficiently implemented so that the corresponding core calculation is parallelized inside the graphics processing unit (GPU) for high-speed applications.⁹ Therefore, this technique is attracting more and more attention from both academia and industry.^{10,11}

The error sources affecting surface reconstruction based on PSA and some variants have been extensively studied. For instance, with a Taylor series expansion, Brophy considered the effect of the intensity fluctuations on PSA.¹² Using Fourier analysis, de Groot analyzed the effect of mechanical vibrations and phase shift error.¹³ Deck corrected the phase error in PSA through a spectral analysis of the error pattern due to vibration.¹⁴ Wang and Han proposed a random PSA to extract the phase distributions with randomly shifted sinusoidal patterns.¹⁵ Chen et al. presented a phase error compensation method to reduce the phase error and shape waviness based on a smoothing spline fitting.¹⁶ Gai and Da combined PSA with amplitude modulation to solve the phase wrapping problem.¹⁷ Last but not least, to improve the accuracy of the reconstruction results and apply PSA in a high-precision

semiconductor inspection, Deng et al. investigated the locally smoothing property of the surface in a regularized phase-shifting algorithm (R-PSA).¹⁸

However, most of these advances in PSA are based on a conventional phase-measuring profilometry model, which assumes that the object for surface reconstruction is stationary, so that each point on the surface receives a consistent illumination during imaging. However, keeping the object stationary is not sufficient to deliver a high throughput in most real-time inspection and measurement applications. For example, on the production line, an object often moves along a conveyor belt and appears at different positions of the field of view (FOV) in the image sequences. As such, uneven illumination becomes more pronounced, especially in camera systems with a large FOV that aim to deliver a high throughput, and the object receives significantly different illumination patterns in the image sequences when moving to different positions. This uneven illumination challenges the conventional model and PSA for surface reconstruction. To cope with this, in this work we propose an illumination-reflectivity-focus (IRF) model to characterize the uneven illumination on phase-measuring profilometry. Concurrent with this, we develop an illumination-invariant phase-shifting algorithm (II-PSA) to reconstruct the surface of a moving object under uneven illumination.

In Sec. 2, we describe the uneven illumination effect on phase-measuring profilometry and review briefly the methods that have been developed to handle this problem. Next, we investigate the intensity formation model mathematically in order to explain why the conventional model fails in reconstructing the surface of a moving object. With this, we propose an IRF model to characterize the uneven illumination factor on phase-measuring profilometry. In Sec. 3, we propose the corresponding II-PSA to solve the phase reconstruction problem under uneven illumination. We give some experimental results in Sec. 4 and concluding remarks in Sec. 5.

2 Uneven Illumination and the Phase-measuring Profilometry Model

2.1 Issue with Uneven Illumination

Many imaging systems produce nonuniform illumination because of either lens distortion or nonuniformity in light sources such as filament support wires, gas discharge electrodes, and light-emitting diode (LED) heat-sink structures. The movement of an object relative to the illumination source also introduces fluctuations in intensity. However, it is difficult to model the illumination source geometrically when the parameters inside the light source are not clear for most applications. Without the model, the nonuniformity is often challenging for many pattern recognition and machine vision applications.

Figure 1 shows the setup of a triangulation system for phase-measuring profilometry. To illustrate the uneven illumination effect on phase estimation, we put a homogeneous plane on the reference plane of a real optical system and project sinusoidal patterns on to its surface. This results in a fringe image, as shown in Fig. 2(a). If we take one row of the intensity image (marked by the red line), ideally this cross-section intensity profile should be a perfect sinusoidal signal, but in practice it is altered as shown in Fig. 2(b). Now,

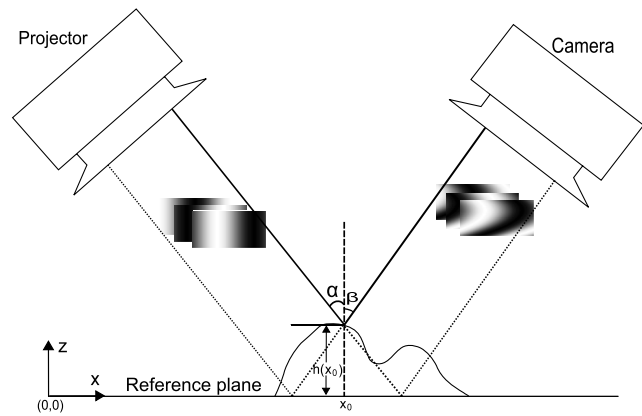


Fig. 1 The schematic setup of the phase reconstruction system.

consider a specific point x_0 , which is shifted by s_k ($k = 1, 2, 3, 4$) along the red line to different positions in the FOV. This cross-section plot also characterizes the intensity profile of x_0 according to the phase shifts from motion. In this example, the points $x_0 + s_k$ correspond to the peaks of the sinusoidal signal. However, their intensities vary due to the uneven illumination distribution on the FOV. This causes significant difficulties in distinguishing such intensity variations from the phase offset due to height variations in phase-measuring profilometry, which becomes a major error source in PSA.

2.2 Methods to Address Illumination Nonuniformity

There are so-called active and passive techniques to tackle illumination nonuniformity. In the former, we add specific illumination sources and sensors to obtain different modalities of the images. For example, assuming that the temperature is constant over the size of the object, infrared imagery has been used to obtain uniform intensity in some vision applications.¹⁹ This assumption, however, may not be valid for general surfaces. Other components, such as optical films and diffusers, can also be used to reduce the uneven illumination,²⁰ which comes at the expense of the overall brightness. Shu et al. proposed a tilted projection optics system to improve the image quality of the fringe pattern.²¹ Another alternative is to use a lens array to improve the illumination evenness,²² but the tradeoff is a more complicated design for the optical system.

In the passive approaches, the illumination variation model requires many testing samples under different lighting conditions to characterize the radiance distribution, or it requires the exact parameters of the components such as the shapes and sizes of the emitting die inside the LED sources. In addition, some emission characteristics, such as a Lambertian object surface, are assumed²³ but these assumptions may not be valid in practical applications. Because of such difficulties, in phase-measuring profilometry, there are not many discussions regarding how to model the illumination variation based on fringe images and how to handle it during surface reconstruction.

2.3 Conventional Phase-Measuring Profilometry Model

Here we briefly review the conventional imaging model. Since the phase is calculated point by point, for simplicity,

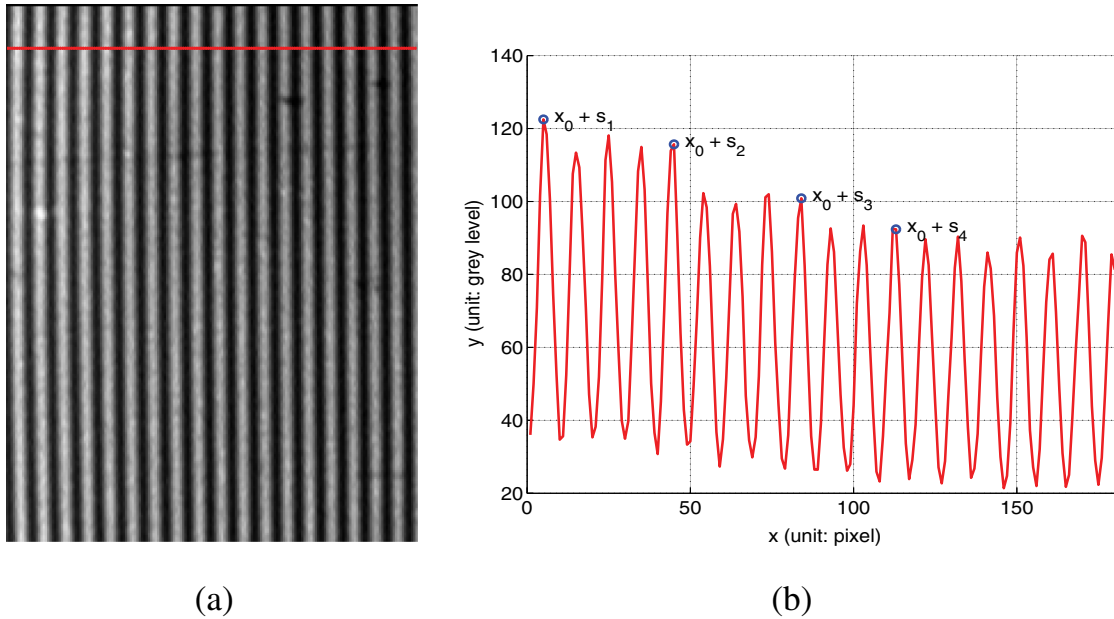


Fig. 2 The fringe pattern on a homogeneous reference plane from a real system under uneven illumination. (a) The projected 2D fringe pattern on the plane. (b) A cross-section intensity profile as indicated in (a) (red line). When a point x_0 on the homogeneous plane moves along this profile, its intensity is altered according to the position $x_0 + s_k$.

we consider only the reconstruction of the height at coordinates x_0 (a two-dimensional quantity in reality) as shown in Fig. 1. We further assume that the phase is shifted along the x -direction. The whole surface reconstruction can then be achieved row by row.¹⁸ If both the projecting and imaging systems are telecentric, we can relate the surface height $h(x_0)$ and the corresponding phase offset $\phi_h(x_0)$ by

$$\phi_h(x_0) = \frac{2\pi(\tan \alpha + \tan \beta)}{P} h(x_0), \quad (1)$$

where P is the pitch of the grating on the reference surface, and α and β are the incident angles of the projector and the detector, respectively.²⁴ This phase offset, $\phi_h(x_0)$, is added to a reference surface phase $\phi_r(x_0)$ to become the total phase of the deformed sinusoidal signal, denoted $\phi(x_0, h)$. That is, $\phi(x_0, h) = \phi_r(x_0) + \phi_h(x_0)$.

Let $B(x_0)$ be the background intensity and $C(x_0)$ be the fringe contrast at the point x_0 . The k th captured image intensity $I_k(x_0)$, at phase shift $\theta(s_k)$ is characterized by

$$I_k(x_0) = B(x_0) + C(x_0) \cos[\phi(x_0, h) + \theta(s_k)] + N_k(x_0), \quad (2)$$

where $k = 1, \dots, n$, and $N_k(x_0)$ is the additive noise. In this equation, there are only three variables: $B(x_0)$, $C(x_0)$, and $\phi(x_0, h)$. Therefore, we need at least three images to solve for them. In practice, it is common to use four (or more) images with evenly distributed phase shifts at $\theta(s_k) = (k-1)\pi/2$, where a simple solution exists, given by

$$\phi_h(x_0) = \arctan \left\{ \frac{I_4(x_0) - I_2(x_0)}{I_1(x_0) - I_3(x_0)} \right\} - \phi_r(x_0). \quad (3)$$

The height is then recovered with Eq. (1), and the whole surface of an object can be obtained point by point in an analogous manner.¹⁸

2.4 Illumination-Reflectivity-Focus Model

The above method allows for an efficient reconstruction of stationary objects, but it is not applicable for reconstructing moving objects or for stationary objects larger than the FOV, because the background intensity and fringe contrast vary according to the shift s_k of the object. Instead, here we develop a generalized model that incorporates the illumination factor explicitly, restricting ourselves to industrial applications where the lighting can be well controlled so that the illumination within each image is a repeatable pattern. Accordingly, we can calibrate the system before real-time reconstruction.

To reconstruct $h(x_0)$ under uneven illumination, we introduce $B(x_0 + s_k)$ and $C(x_0 + s_k)$ (where $k = 1, \dots, n$) in the phase-measuring model when the point is shifted to $x_0 + s_k$. The intensity $I_k(x_0)$ can then be described as

$$I_k(x_0) = B(x_0 + s_k) + C(x_0 + s_k) \cos[\phi(x_0, h) + \theta(s_k)] + N_k(x_0). \quad (4)$$

Furthermore, we decompose these two new variables in terms of the reflectivity factor $R(x_0)$, which is a constant irrespective of the shift, the illumination factor $L(x_0 + s_k)$, and the focus factor $F(x_0 + s_k)$, such that

$$B(x_0 + s_k) = L(x_0 + s_k)R(x_0), \quad (5)$$

$$C(x_0 + s_k) = L(x_0 + s_k)R(x_0)F(x_0 + s_k). \quad (6)$$

This leads to our illumination-reflectivity-focus (IRF) model, where

$$I_k(x_0) = L(x_0 + s_k)R(x_0)\{1 + F(x_0 + s_k) \cos[\phi(x_0, h) + \theta(s_k)]\} + N_k(x_0). \quad (7)$$

There are several advantages of this IRF model:

- *The IRF model identifies the three major factors for formulating and analyzing the intensity images.* Eq. (7) points out that the three major factors contributing to the intensity image are the illumination, the reflectivity from the surface, and the focus. We can thus consider how each of them affects the image formation, and we can study the error sources from these factors individually.
- *IRF generalizes the conventional model.* When we reconstruct the surface of a stationary object, the illumination and the focus at x_0 are not changed according to the phase shifts. On the other hand, when we reconstruct the surface of a moving object under even illumination and focus, the illumination factor and the focus factor are the same for all s_k , i.e., $L(x_0) = L(x_0 + s_k)$ and $F(x_0) = F(x_0 + s_k)$. In these two special cases, the conventional model in Eq. (2) suffices. However, in a large FOV system with varying illumination and focus distributions, we need to turn to this generalized IRF model to describe the exact relationship between the phase offset due to the height variation and the deformed intensity, as well as to reconstruct the surface of the moving objects.
- *The decomposition suggests an efficient way to tackle the phase reconstruction problem.* When the optical system is fixed, the illumination on the FOV remains the same during image formation. Because this IRF model separates it from the other factors, we can calibrate the illumination distribution first and then use this as prior knowledge during the real-time surface reconstruction.

In the following section, we show how to formulate the phase reconstruction as an optimization problem based on this IRF model.

3 Problem Formulation and Illumination-Invariant Phase-Shifting Algorithm

To simplify the discussion, we use a four-frame algorithm with phase shifts at $\theta(s_k) = (k - 1)\pi/2$ as an example while noting that the present method is applicable to other cases with more frames and shifts. Consider the phase reconstruction at a specific point x_0 . Let $E_k(x_0)$ be the residual error of the model in Eq. (7), i.e.,

$$E_k(x_0) = I_k(x_0) - L(x_0 + s_k)R(x_0) \times \left\{ 1 + F(x_0 + s_k) \cos \left[\phi(x_0, h) + (k - 1) \frac{\pi}{2} \right] \right\}, \quad (8)$$

and the optimal $\phi(x_0, h)$ at x_0 is found by minimizing

$$E(x_0) = \sum_{k=1}^4 E_k^2(x_0). \quad (9)$$

With the IRF model, the degrees of freedom exceed the

amount of data we collect, so it is a challenge to solve for $\phi(x_0, h)$ without prior knowledge.

We note, however, that the case is made simpler if the projecting and imaging systems are fixed. Although the illumination and the focus vary according to their positions in this IRF model, their distributions on the FOV remain the same when we reconstruct the surface of the moving objects. Therefore, we can use a homogeneous reference plane for calibration beforehand. Without loss of generality, we assume the reflectivity is unity on such a reference plane, where $\phi_h(x_0) = 0$ for all x_0 , and therefore $\phi(x_0, h) = \phi_r(x_0)$. After we shift the grating regularly with phase shifts $\theta(s_k) = (k - 1)\pi/2$, we can calculate $\phi_r(x_0)$ from Eq. (3) point by point, which becomes the reference phase for later use.

Next we compute the illumination and focus distributions. By substituting the reference phase as $\phi(x_0, h)$ in Eq. (2), and denoting

$$M_0 = \begin{bmatrix} 1 & \cos(\phi(x_0, h) + 0) \\ 1 & \cos(\phi(x_0, h) + \frac{\pi}{2}) \\ 1 & \cos(\phi(x_0, h) + \pi) \\ 1 & \cos(\phi(x_0, h) + \frac{3\pi}{2}) \end{bmatrix}, \quad (10)$$

and

$$\mathbf{v}_0 = \begin{bmatrix} B(x_0) \\ C(x_0) \end{bmatrix}, \quad \mathbf{n}_0 = \begin{bmatrix} N_1(x_0) \\ N_2(x_0) \\ N_3(x_0) \\ N_4(x_0) \end{bmatrix}, \quad \mathbf{i}_0 = \begin{bmatrix} I_1(x_0) \\ I_2(x_0) \\ I_3(x_0) \\ I_4(x_0) \end{bmatrix}, \quad (11)$$

we have a simple matrix form $M_0\mathbf{v}_0 + \mathbf{n}_0 = \mathbf{i}_0$ for the imaging model. Assuming that the noise is additive Gaussian, we can use least squares to estimate $B(x_0)$ and $C(x_0)$ by minimizing $\|M_0\mathbf{v}_0 - \mathbf{i}_0\|_2^2$.

We note, however, that the camera noise and quantization error cause these least-square solutions to fluctuate significantly. In most practical systems for machine vision applications, the illumination varies gradually within a small neighborhood. Hence, we apply a lowpass filter (such as a 3×3 simple averaging) to these point-wise $B(x_0)$ and $C(x_0)$. With these, the illumination and focus distributions can be estimated from Eqs. (5) and (6).

Next we proceed to phase recovery. When we place the reconstruction point x_0 at different positions in the FOV under uneven illumination, the values of the cost function represented by Eqs. (8) and (9) are different. However, the surface properties of this point, namely its reflectivity and height, are related only to the variables $R(x_0)$ and $\phi(x_0, h)$. In a calibrated system with known illumination and focus distributions, these two variables model the magnitude modulation and the phase modulation processes, respectively, and they uniquely determine the intensity images at a given phase shift. Therefore, even if more images are captured for the sake of robustness and accuracy, the degrees of freedom remain at two in this calibrated system. As such, we name these two the fundamental variables.

Furthermore, we make use of a different cost function that is invariant to illumination and focus distributions. This is achieved through normalizing the original cost function by the illumination and focus quantities. Then the new cost function is

$$\hat{E}(x_0) = \sum_{k=1}^4 \left\{ \frac{I_k(x_0)}{L(x_0 + s_k)F(x_0 + s_k)} - \frac{R(x_0)}{F(x_0 + s_k)} - R(x_0) \cos \left[\phi(x_0, h) + (k-1) \frac{\pi}{2} \right] \right\}^2. \quad (12)$$

Note that the illumination and focus distributions are known within the FOV after the previous optical calibration step, so there are only two variables to be optimized: $R(x_0)$ and $\phi(x_0, h)$. Since they are coupled in this nonlinear optimization problem, to handle them one at a time, we first consider $R(x_0)$, $R(x_0) \cos \phi(x_0, h)$, and $R(x_0) \sin \phi(x_0, h)$ as variables and solve for them through a least-square estimation. Then, based on this estimated $R(x_0)$, we compute the optimal $\phi(x_0, h)$ in a manner similar to our previous work.²⁴

For simplicity, we denote the calibrated $L(x_0 + s_k)$ and $F(x_0 + s_k)$ as L_k and F_k , respectively, and we let

$$\hat{M}_0 = \begin{bmatrix} \frac{1}{F_1} & \cos 0 & -\sin 0 \\ \frac{1}{F_2} & \cos \frac{\pi}{2} & -\sin \frac{\pi}{2} \\ \frac{1}{F_3} & \cos \pi & -\sin \pi \\ \frac{1}{F_4} & \cos \frac{3\pi}{2} & -\sin \frac{3\pi}{2} \end{bmatrix}, \quad (13)$$

and

$$\hat{v}_0 = \begin{bmatrix} R(x_0) \\ R(x_0) \cos \phi(x_0, h) \\ R(x_0) \sin \phi(x_0, h) \end{bmatrix}, \quad \hat{i}_0 = \begin{bmatrix} \frac{I_1(x_0)}{L_1 F_1} \\ \frac{I_2(x_0)}{L_2 F_2} \\ \frac{I_3(x_0)}{L_3 F_3} \\ \frac{I_4(x_0)}{L_4 F_4} \end{bmatrix}. \quad (14)$$

Minimizing the cost function in Eq. (12) can therefore be formulated as minimizing

$$\hat{E}(x_0) = \left\| \hat{M}_0 \hat{v}_0 - \hat{i}_0 \right\|_2^2. \quad (15)$$

Using a least-square estimation, we have

$$\hat{v}_0 = (\hat{M}_0^T \hat{M}_0)^{-1} \hat{M}_0^T \hat{i}_0. \quad (16)$$

We can now extract the first element $R(x_0)$ from \hat{v}_0 , substitute this variable into Eq. (12), and then solve for the more important variable $\phi(x_0, h)$ related to the surface height. With known L_k , F_k , and $R(x_0)$, letting

$$\tilde{M}_0 = \begin{bmatrix} R(x_0) \cos 0 & -R(x_0) \sin 0 \\ R(x_0) \cos \frac{\pi}{2} & -R(x_0) \sin \frac{\pi}{2} \\ R(x_0) \cos \pi & -R(x_0) \sin \pi \\ R(x_0) \cos \frac{3\pi}{2} & -R(x_0) \sin \frac{3\pi}{2} \end{bmatrix}, \quad (17)$$

and

$$\tilde{v}_0 = \begin{bmatrix} \cos \phi(x_0, h) \\ \sin \phi(x_0, h) \end{bmatrix}, \quad \tilde{i}_0 = \begin{bmatrix} \frac{I_1(x_0)}{L_1 F_1} - \frac{R(x_0)}{F_1} \\ \frac{I_2(x_0)}{L_2 F_2} - \frac{R(x_0)}{F_2} \\ \frac{I_3(x_0)}{L_3 F_3} - \frac{R(x_0)}{F_3} \\ \frac{I_4(x_0)}{L_4 F_4} - \frac{R(x_0)}{F_4} \end{bmatrix}, \quad (18)$$

we can minimize the cost function in Eq. (12) by reformulating it to

$$\begin{aligned} \text{minimize} \quad & \hat{E}(x_0) = \left\| \tilde{M}_0 \tilde{v}_0 - \tilde{i}_0 \right\|_2^2, \\ \text{subject to} \quad & \left\| \tilde{v}_0 \right\| = 1. \end{aligned} \quad (19)$$

This is solved by a standard least-square optimization with a quadratic constraint.²⁵

After obtaining the optimized $\cos \phi(x_0, h)$ and $\sin \phi(x_0, h)$ from \tilde{v}_0 , we can determine the phase $\phi(x_0, h)$. Finally, by subtracting the reference phase $\phi_r(x_0)$ from the calibration, we can use Eq. (1) to obtain the surface profile point by point.

4 Numerical Analyses and Experiments

4.1 Simulation Experiments

In the experiments below, we extract four consecutive images from a synthetic image sequence and apply the four-frame PSA and II-PSA with phase shifts $\theta(s_k) = (k-1)\pi/2$ for surface reconstruction. Figure 3(a) to 3(d) shows one set of the sample images of a homogeneous plane when it moves along the x -direction across the FOV of the optical system. The period of the sinusoidal pattern is $P = 12$ pixels, and the images are captured at four sequential positions at $s_1 = 0$, $s_2 = 63$, $s_3 = 126$, and $s_4 = 189$ pixels relative to the initial position. The red boxes mark the region of interest (ROI) on the plane when it moves to different positions of the FOV. We align these ROIs from the image sequences as shown in 3(e) to 3(h) before surface reconstruction. Note that we can see, for instance, that 3(e) is brighter than 3(h), indicating uneven illumination during the imaging process.

In our first experiment, the illumination distribution is synthesized linearly from an intensity level 100 on the left end of a 256×256 image to 50 on the right. The focus factor is assumed to be a constant equal to 0.8 on a homogeneous plane. We synthesize these images according to the IRF model in Eq. (7), together with an additive Gaussian noise with a standard deviation of 5. After calibrating the illumination and focus distributions, we reconstruct the phase due to height variations, where a set of one-dimensional reconstruction results are shown in Fig. 4. Figure 4(a) shows the four cross-section intensity profiles extracted from the center rows of the aligned ROIs in Fig. 3. We can observe that the uneven illumination contributes significantly to the nonuniformity of the sinusoidal signal, compared with the camera noise. This variation would normally be interpreted as a phase offset due to the height variation in PSA, and it causes a large periodic phase error disturbance on the reconstructed phase, as shown in (b). In contrast, in our II-PSA, this periodic error pattern is removed by illumination normalization.

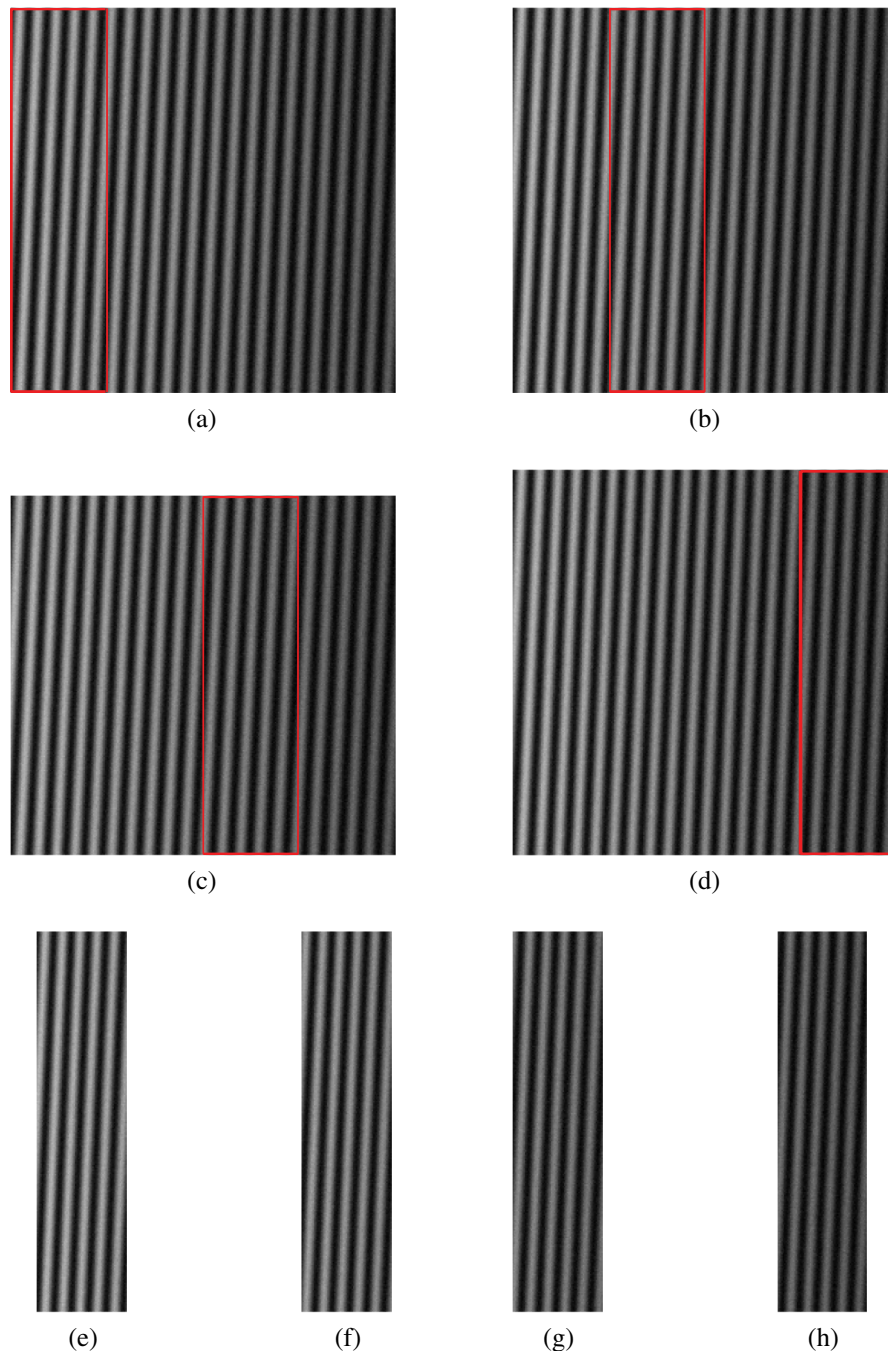


Fig. 3 (a) to (d) The image sequences of a homogeneous plane moving horizontally from left to right. (e) to (h) The corresponding regions of interest extracted from these images. These regions come from the same physical region of the object during the movements, and they are aligned for surface reconstruction.

Only a random error pattern due to the camera noise remains. The standard deviations of the error are 0.23 radian for PSA and 0.07 radian for II-PSA, respectively.

Our next experiments involve the two-dimensional model under different illumination distributions. Similar to the above experiment, we simulate the illumination distribution, now a two-dimensional function denoted $L(x, y)$, by using different analytical functions, such as a linear function [where $L(x, y) = 100 - 0.2x$], a quadratic function {where $L(x, y) = 100 - [(x-128)/26]^2 + (y-128)/26^2$ }, and a Gaussian

function {where $L(x, y) = 100 \exp[-((x-128)/220)^2 + ((y-128)/220)^2]$ }. To test the performances at different phase values, we synthesize a tilted plane with the ground truth phase offsets from $-\pi$ to π when forming the intensity images. Figure 5 shows one sample result based on the quadratic illumination pattern and an additive Gaussian noise with a standard deviation of 5. As we compare PSA with II-PSA, again we can see that the periodic error disturbance is significantly suppressed in the latter. More quantitative results at different noise levels are given in Table 1.

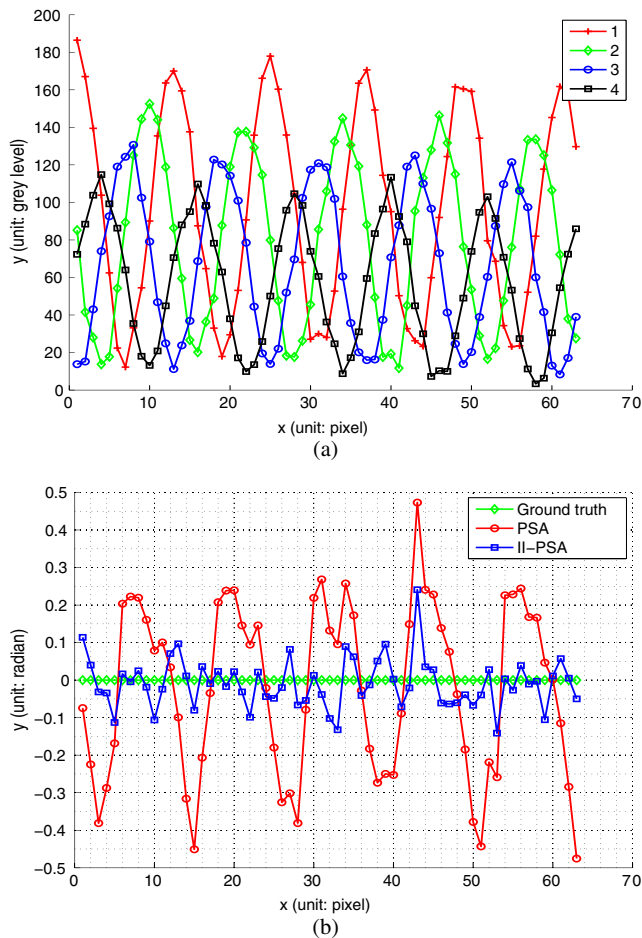


Fig. 4 Reconstruction results based on a one-dimensional model. (a) Four synthetic intensity profiles at phase shifts $\theta(s_k) = (k-1)\pi/2$. (b) The reconstruction results from PSA and II-PSA.

In addition to noting that II-PSA in general gives a smaller error than PSA, we can also observe that the reconstruction performance of II-PSA under different illumination distributions are quite close at the same noise level. This trend is even more evident at a low noise level when the uneven illumination becomes more pronounced than the camera noise. This points to the fact that the cost function in II-PSA is invariant to illumination distributions. Further, when the noise intensity is small, such as when $\sigma = 1$, the improvement of our II-PSA over PSA is very significant. The standard deviation of the error is only 0.01 radian under different illumination distributions. As the noise level increases, the improvement of our II-PSA becomes less pronounced, because the camera noise has a dominant effect on the intensity fluctuation and becomes a major error source. The benefit of calibrating and correcting the uneven illumination distribution is reduced.

4.2 Experiments in Real Applications

We have applied the surface reconstruction technique in a machine vision system for inspecting surfaces of thin solar wafers. These wafers are crisp and easily stained during production. For solar panel efficiency consideration in solar energy applications, the precise dimensional information—especially the thickness of wafers—must remain within a

certain range. Also, for monitoring the quality of the wafers on the production line, we need to check whether there are defects on these wafers by inspecting their 3D surfaces.

Figure 6(a) shows a typical polycrystal wafer image captured by a color camera. Since the wafer is large (around 156 mm by 156 mm) and very thin (around 200 μm), it is easy to break it and difficult to use conventional metrology tools to measure its surface without staining it. To reconstruct the dense surfaces of this wafer efficiently on the production line for subsequent surface inspection and height measurement, we have designed an automated noncontact phase-measuring profilometry system. In our system, we adopt the cameras and projectors made by ASM Pacific Technology Limited. The frame rate of the camera is 100 frames per second, and these CCD cameras output eight-bit-intensity images with an array size of 240×240 at each frame. Since the imaging resolution is 27 μm per pixel along the moving direction x and 235 μm per pixel along the y -direction, the resulting FOV for each image is only 6.48 mm by 56.4 mm. To reconstruct the top view surface of the wafer when it moves along the x -direction, we use three pairs of cameras and projectors. We arrange these cameras and projectors along the y -direction in a triangular setup as shown in Fig. 6(b), so they can always cover the wafer in the y -direction and reconstruct piece by piece along the x -direction. Similarly, we use another three pairs of cameras and projectors below the wafer to reconstruct the bottom view surface of the wafer.

Using the conventional phase-shifting algorithm, we find there is a periodic error disturbance of about $\pm 15 \mu\text{m}$ in the reconstructed wafer surface as shown in Fig. 7. Figure 7(a) shows a real sample image of a polycrystal wafer with an image size of 240×240 pixels. This image is captured by the middle camera on the top after projecting sinusoidal patterns on the wafer. From this fringe image, we can easily observe the uneven illumination effect, because the left side of the FOV is brighter than the right side. As analyzed in Sec. 2, this uneven illumination pattern introduces error in the phase-measuring profilometry, and it affects the subsequent inspection and measurement. However, once the optical system has been installed and fixed on the production line, this uneven illumination pattern is repeatable. To remove this error source, first we use the proposed II-PSA from Sec. 3 to calibrate the illumination pattern. As shown in Fig. 6(b), a wafer is kept stationary within the FOV of the optical system for calibration. Afterwards, we normalize this illumination pattern during the real-time surface reconstruction when the wafers are moving along the conveyor belt during the production process. Figure 7(b) and 7(c) shows the reconstructed profiles of the region marked on the image of the wafer in Fig. 7(a) based on the conventional PSA and our II-PSA. By comparing these reconstructed surfaces and their cross-section 1D profiles as shown in Fig. 7(d), we can see that, using our technique, the periodic error pattern caused by the uneven illumination can be removed. And we have achieved an accuracy of less than 10 μm in our reconstruction system. For high-speed consideration, besides using multiple cameras and projectors, we use Intel(R) Core (TM) i7 CPU X 980 @ 3.33 GHz with 4 G RAM in our system, so that we can reconstruct a wafer within 1 s and apply our system in real-time solar wafer inspection on the production line.

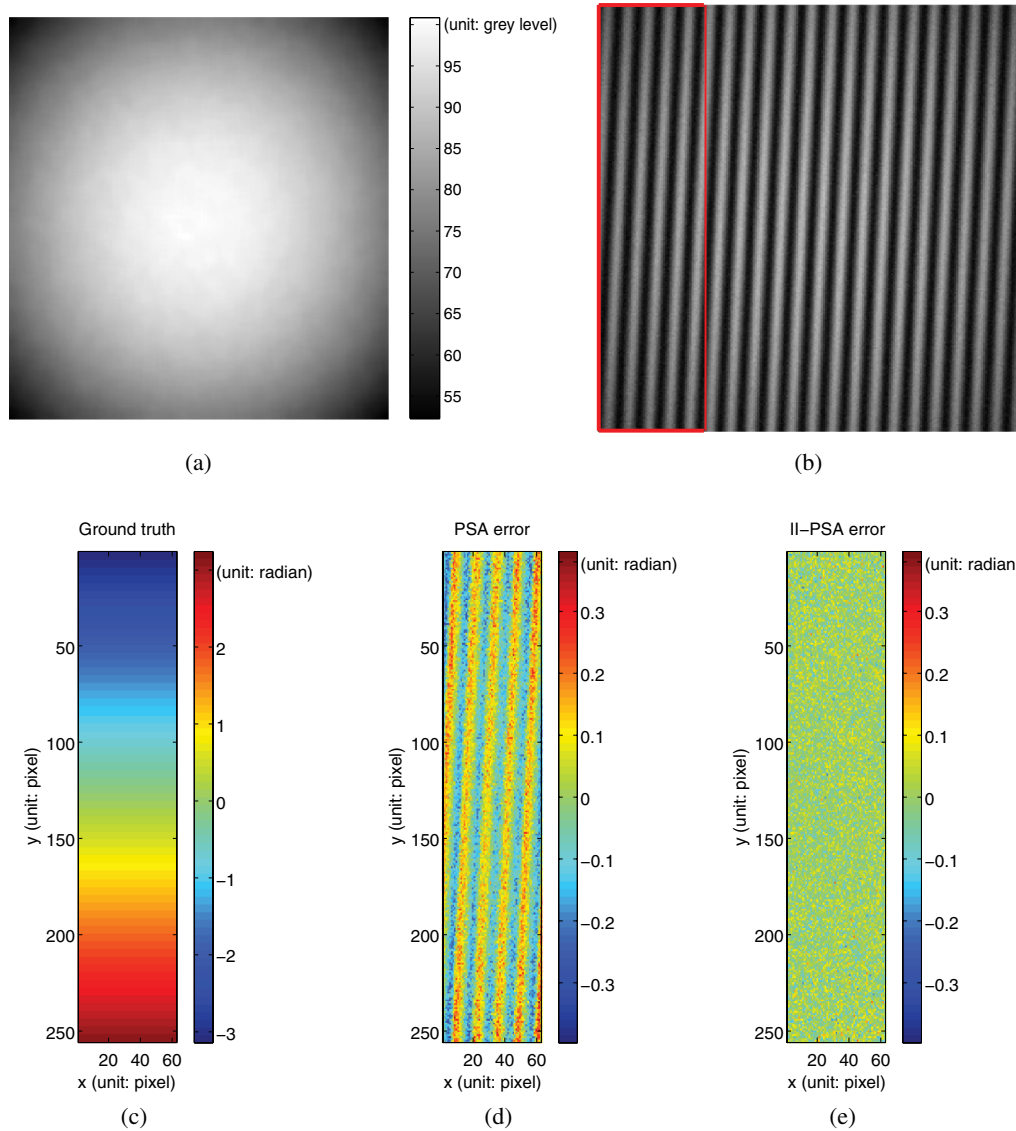


Fig. 5 Reconstruction results based on a two-dimensional model. (a) The calibrated illumination pattern. (b) One of the fringe images for reconstruction. (c) The synthetic phase. (d) and (e) The errors during reconstruction from PSA and II-PSA, respectively.

Table 1 Standard deviations σ of the reconstruction error under different uneven illumination distributions (unit: radian).

		Noise level				
		$\sigma = 1$	$\sigma = 3$	$\sigma = 5$	$\sigma = 10$	$\sigma = 15$
$L(x, y) = 100 - 0.2x$	PSA	0.22	0.22	0.23	0.25	0.29
	II-PSA	0.01	0.04	0.06	0.12	0.19
$L(x, y) = 100 - \left[\left(\frac{x-128}{26}\right)^2 + \left(\frac{y-128}{26}\right)^2\right]$	PSA	0.11	0.11	0.12	0.15	0.19
	II-PSA	0.01	0.03	0.05	0.10	0.16
$L(x, y) = 100 \exp\left[-\left(\frac{x-128}{220}\right)^2 - \left(\frac{y-128}{220}\right)^2\right]$	PSA	0.12	0.12	0.13	0.16	0.21
	II-PSA	0.01	0.03	0.06	0.11	0.17

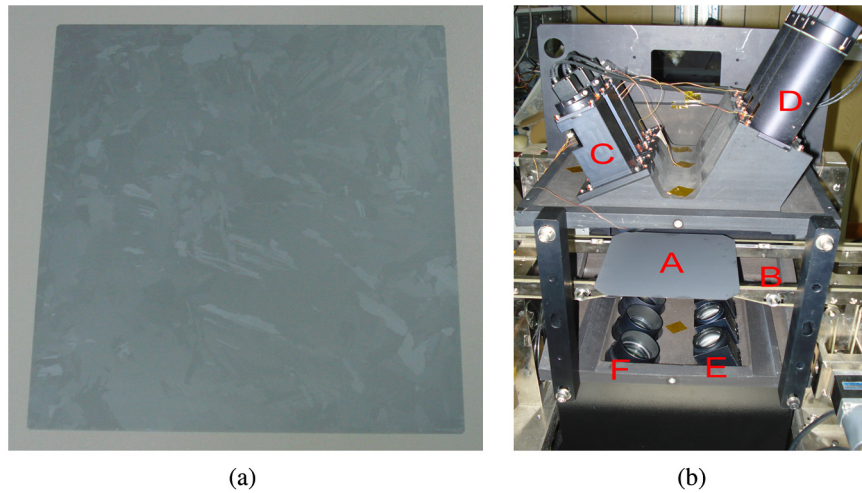


Fig. 6 A real surface reconstruction system is applied in the semiconductor industry for solar wafer inspection. (a) A color picture of a typical polycrystalline wafer. To qualify the wafer before solar energy application, we need to reconstruct its surface for inspection. (b) The physical setup of our surface reconstruction system. A: wafer under inspection, B: conveyor belt for transferring wafers, (c) camera arrays for top view reconstruction, (d) projector arrays for top view reconstruction, E: camera arrays for bottom view reconstruction, F: projector arrays for bottom view reconstruction. When a wafer enters our system through the conveyor belt, the top view cameras capture the sinusoidal patterns from the corresponding projectors for reconstructing the top surface of the wafer. Similarly, the bottom view cameras and projectors are used for reconstructing the bottom surface of the wafer.

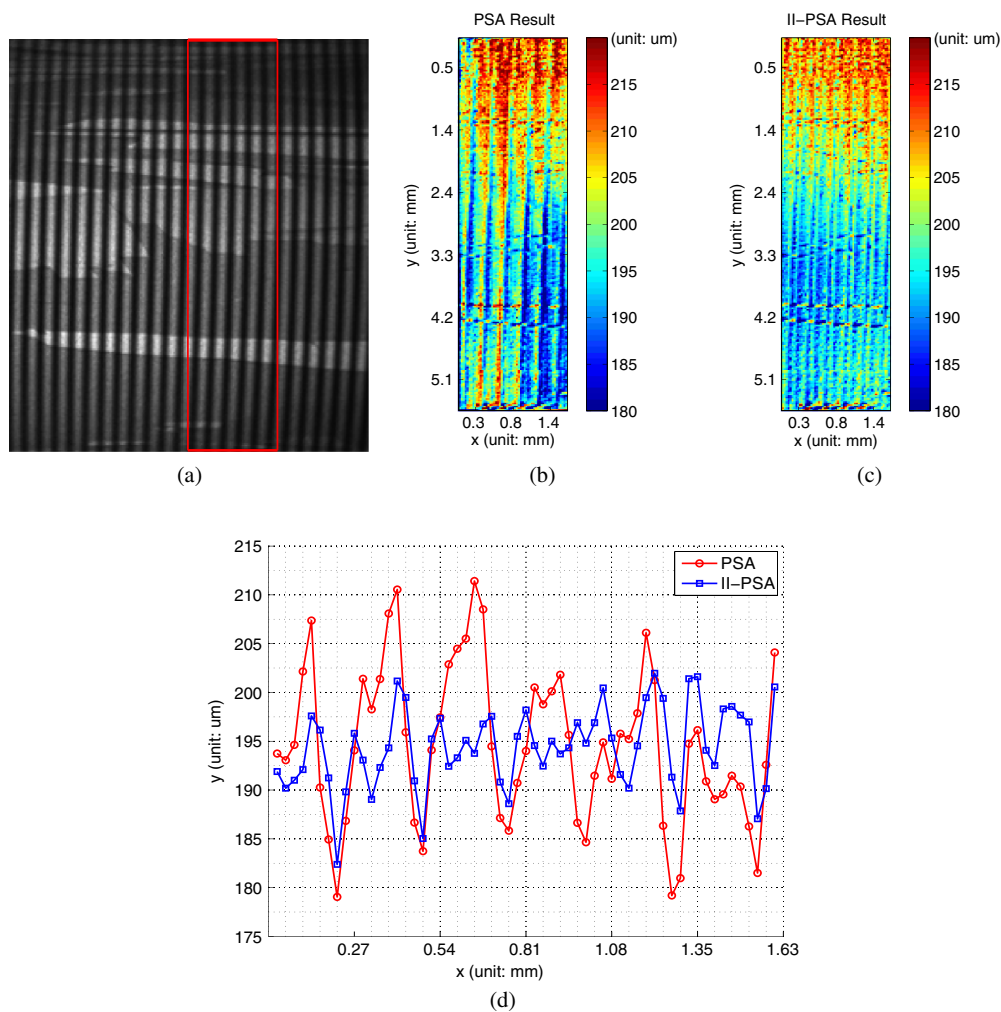


Fig. 7 The comparison of the reconstruction results with PSA and II-PSA. (a) One of the fringe images on a polycrystalline wafer; the marked region is the current reconstruction region. (b) The reconstructed profile from PSA. (c) The reconstructed profile from II-PSA. (d) The 1D cross-section profiles from the middle rows of the profiles in (b) and (c).

5 Conclusions

In this paper and its earlier conference version,²⁶ we propose an IRF model to characterize the uneven illumination factor for phase-measuring profilometry, and we develop an II-PSA to reconstruct the surface profile of moving objects. When uneven illumination is a dominant error source in phase-measuring profilometry, such as in our solar wafer inspection system, we can calibrate the illumination distribution beforehand based on this novel IRF model. Then we can use the proposed II-PSA to remove the periodic error pattern introduced by the uneven illumination. Experimental results show that our algorithm can significantly improve the reconstruction quality both visually and numerically.

Acknowledgments

This work and its earlier conference version are supported in part by ASM Pacific Technology Limited and by the University Research Committee of the University of Hong Kong under Project 10208648.

References

1. F. Chen, G. M. Brown, and M. Song, "Overview of three-dimensional shape measurement using optical methods," *Opt. Eng.* **39**(1), 10–22 (2000).
2. A. N. Ng et al., "Reference-free machine vision inspection of semiconductor die images," *Int. J. Image Graphics* **9**(1), 133–152 (2009).
3. T. Wakayama and T. Yoshizawa, "Compact camera for three-dimensional profilometry incorporating a single mems mirror," *Opt. Eng.* **51**(1), 013601 (2012).
4. M. Dong et al., "Height inspection of wafer bumps without explicit 3D reconstruction," *IEEE Trans. Electron. Packaging Manuf.* **33**(2), 112–121 (2010).
5. J. Cheng et al., "Structure-light based sensing using a single fixed fringe grating: Fringe boundary detection and 3D reconstruction," *IEEE Trans. Electron. Packaging Manuf.* **31**(1), 19–31 (2008).
6. S. Zhang and S.-T. Yau, "High-resolution, real-time 3D absolute coordinate measurement based on a phase-shifting method," *Opt. Express* **14**(7), 2644–2649 (2006).
7. J. Cheng et al., "Optimization of bit-pairing codification with learning for 3D reconstruction," *Int. J. Image Graphics* **7**(3), 445–462 (2007).
8. R. Chung et al., "Imaging system for three-dimensional reconstruction of surface profiles," U. S. Patent No. 7,676,114 (2010).
9. S. Zhang, D. Royer, and S.-T. Yau, "GPU-assisted high-resolution, real-time 3-D shape measurement," *Opt. Express* **14**(20), 9120–9129 (2006).
10. F. Blais, "Review of 20 years of range sensor development," *J. Electron. Imag.* **13**(1), 231–240 (2004).
11. S. S. Gorthi and P. Rastogi, "Fringe projection techniques: Whither we are?," *Opt. Lasers Eng.* **48**(2), 133–140 (2010).
12. C. P. Brophy, "Effect of intensity error correlation on the computed phase of phase-shifting interferometry," *J. Opt. Soc. Am. A* **7**(4), 537–541 (1990).
13. P. J. de Groot, "Vibration in phase-shifting interferometry," *J. Opt. Soc. Am. A* **12**(2), 354–365 (1995).
14. L. L. Deck, "Suppressing phase errors from vibration in phase-shifting interferometry," *Appl. Opt.* **48**(20), 3948–3960 (2009).
15. Z. Wang and B. Han, "Advanced iterative algorithm for phase extraction of randomly phase-shifted interferograms," *Opt. Lett.* **29**(14), 1671–1673 (2004).
16. X. Chen, J. Xi, and Y. Jin, "Phase error compensation method using smoothing spline approximation for a three-dimensional shape measurement system based on gray-code and phase-shift light projection," *Opt. Eng.* **47**(11), 113601 (2008).
17. S. Gai and F. Da, "Fringe image analysis based on the amplitude modulation method," *Opt. Express* **18**(10), 10704–10719 (2010).
18. F. Deng and E. Y. Lam, "Three-dimensional surface recovery with a regularized multi-frame phase shift algorithm," *OSA Topical Meeting in Signal Recovery and Synthesis, SMD3* (2011).
19. S. G. Kong et al., "Recent advances in visual and infrared face recognition: a review," *Computer Vision and Image Understanding* **97**(1), 103–135 (2005).
20. E. R. Méndez et al., "Photofabrication of random achromatic optical diffusers for uniform illumination," *Appl. Opt.* **40**(7), 1098–1108 (2001).
21. Y. Shu et al., "Projection optics design for tilted projection of fringe pattern," *Opt. Eng.* **47**(5), 053002 (2008).
22. J. P. Peck and C. V. Shastry, "LED lens array optic with a highly uniform illumination pattern," U. S. Patent No. 0,002,985 A1 (2009).
23. X. Zou, J. Kittler, and K. Messer, "Illumination invariant face recognition: a survey," presented at *IEEE First International Conf. on Biometrics: Theory, Applications and Systems*, Crystal City, VA, pp. 1–8 (2007).
24. F. Deng et al., "Regularized multiframe phase-shifting algorithm for three-dimensional profilometry," *Appl. Opt.* **51**(1), 33–42 (2012).
25. Å. Björck, *Numerical Methods for Least Squares Problems*, Society for Industrial and Applied Mathematics, Philadelphia, PA (1996).
26. F. Deng et al., "An illumination-invariant phase-shifting algorithm for three-dimensional profilometry," *Proc. SPIE* **8300**, 830005 (2012).



Fuqin Deng received a BS in applied mathematics from Harbin Institute of Technology, Harbin, China, in 2005 and an MS in control science and engineering from the Shenzhen Graduate School of Harbin Institute of Technology, Shenzhen, China, in 2007. Currently he is a PhD student in the Department of Electrical and Electronic Engineering at the University of Hong Kong. His research interests include image processing, pattern recognition, and computer vision.



Chang Liu received a BS in information systems from Nankai University, Tianjin, China, in 2003, an MS in applied mathematics from Sun Yat-Sen University, Guangzhou, China, in 2006, and a PhD degree from the Department of Computer Science of Hong Kong Baptist University, Kowloon, Hong Kong. His research interests include pattern recognition, computer vision, and machine learning.



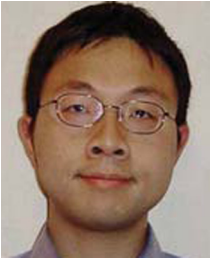
Wufung Sze received a BEng in electronic and communications engineering (1st class honor) and MPhil and MStat (distinction) degrees from the University of Hong Kong. He worked as a system engineer at Octopus Card Limited before joining ASM Pacific Technology Limited, where he is now a senior electronic engineer responsible for developing high-precision 3D measurement applications.

Jiangwen Deng is a technical manager in the Research and Development Department at ASM Pacific Technology Limited.



Kenneth S. M. Fung is a technical manager in the Research and Development Department at ASM Pacific Technology Limited. After receiving a PhD in 1999 from the Department of Electrical and Electronic Engineering at the University of Hong Kong, he joined ASM Pacific Technology Limited as a senior engineer. He developed a subpixel-accuracy, high-speed, and robust computer vision alignment algorithm that was applied in all ASM products and boosted the capability and vision technology level of the company's semiconductor packaging machines. He leads a team of research engineers responsible for projects in machine vision inspection and algorithm development. He also provides technical supervision for a team of vision application engineers responsible for developing machine vision applications on ASM products. His research interests are computer vision, pattern recognition, digital image processing, and artificial neural networks.

W. H. Leung is the technical director in the Research and Development Department at ASM Pacific Technology Limited.



Edmund Y. Lam is an associate professor in electrical and electronic engineering and a codirector of the computer engineering program at the University of Hong Kong. He is also the founding director of its Imaging Systems Laboratory. He has broad research interests around the theme of computational optics and imaging, particularly its applications in semiconductor manufacturing and biomedical systems. He is a topical editor of the Journal of the Optical Society of

America A, an associate editor of the IEEE Transactions on Biomedical Circuits and Systems, and an editorial board member of the Journal of Ambient Intelligence and Smart Environments. He has been a guest editor for the Journal of Electronic Imaging and for Multidimensional Systems and Signal Processing. In 2010, he taught in the Department of Electrical Engineering and Computer Science at Massachusetts Institute of Technology as a visiting associate professor.